Journal of Magnetic Resonance **139,** 81–89 (1999)
Article ID jmre.1999.1749, available online at http://www.idealibrary.com on IDEAL®

An "Openable," High-Strength Gradient Set for Orthopedic MRI

Stuart Crozier, Wolfgang U. Roffmann, Kurt Luescher, Christopher Snape-Jenkinson,*
Lawrence K. Forbes,* and David M. Doddrell

*Centre for Magnetic Resonance and *Department of Mathematics, University of Queensland, Brisbane, Queensland 4072, Australia*

Received September 25, 1998; revised December 29, 1998

A novel three-axis gradient set and RF resonator for orthopedic MRI has been designed and constructed. The set is openable and may be wrapped around injured joints. The design methodology used was the minimization of magnetic field spherical harmonics by simulated annealing. Splitting of the longitudinal coil presents the major design challenge to a fully openable gradient set and in order to efficiently design such coils, we have developed a new fast algorithm for determining the magnetic field spherical harmonics generated by an arc of multiturn wire. The algorithm allows a realistic impression of the effect of split longitudinal designs. A prototype set was constructed based on the new designs and tested in a 2-T clinical research system. The set generated 12 mT/m/A with a linear region of 12 cm and a switching time of 100 μs, conforming closely with theoretical predictions. Preliminary images from the set are presented.

INTRODUCTION

The use of strong gradients with fast rise-times in MRI experiments is often desirable in order to reduce echo times and to decrease off-resonance evolution. Local gradient coils offer distinct advantages in this regard (*1, 2*). For applications in which strong gradients with fast switching times are highly advantageous, such as diffusion tensor imaging (*3*) and fast imaging sequences such as RARE (*4*) and EPI (*5*), we have designed a strong, local gradient set for joint imaging. Orthopedic imaging is further complicated by the limited joint motion by patients with injuries, often preventing the safe and comfortable use of conventional local gradient coils. The gradient set described here is designed to be wraparound or openable, such that the RF coil and gradient set may be applied around the joint under study, thus reducing the amount of suppleness required by the patient.

In this paper we detail the engineering design of the set and present preliminary RARE knee images. An initial account of this work has been presented (*6*).

THEORY

The design of the transverse coils is comparatively straightforward as their symmetry allows the splitting of the pattern around the X or Y axis. A length constrained current density method was used (*7*) with the modest overall length constraints of 415 mm with an internal diameter of 250 mm, giving a length-to-diameter ratio of approximately 1.7. An example of one of the transverse sheet patterns is given in Fig. 1. Special care must be taken to ensure that the sheet patterns are symmetrical around the X and Y axes, with the insertion of two sets of hinges necessitating a trimming of the sheet pattern to ensure this. A lack of cylindrical symmetry generates exaggerated forces and torques when the gradient set is pulsed in the magnet system.

The design of a split longitudinal gradient set is more difficult than the transverse coils and we now present our approach in detail. Conventional Z gradient sets comprise a series of interconnected hoops with odd symmetry in current density (winding direction) about the isocenter. The scheme for the return paths to enable an openable set to be constructed is shown in Fig. 2. In designing gradient sets it is often instructive to consider the spherical harmonics of the magnetic field that the coils generate, as this is a sensitive measure of the purity (linearity) of the generated gradient field.

When modeling conventional Z gradient sets, odd order zonal harmonics are the only significant terms in field expansion, due to the complete cylindrical symmetry of the coils and their odd zonal symmetry. The harmonics generated by the coils may be calculated by first calculating the field on the surface of a sphere in the center of the coil set and then deconvolving into spatial harmonic terms (*8, 9*). The harmonics may be more directly and efficiently evaluated from recursive relationships initially presented for magnet design (*10, 11*). In the case of a split coil system, however, the axial return paths prevent complete azimuthal inclusion and necessitate the derivation of a new algorithm for the efficient calculation of the complete harmonics generated by a multiturn "arc" conductor as shown in Fig. 3. Due to the fact that the current carrying arcs have longitudinal return paths for "splitting," the arcs subtend an angle less than 180° and therefore generate tesseral harmonic components. These components are undesirable and need to be included in the error function to be minimized.

Once the harmonics are derived from the coil structure, the design proceeds by the minimization of harmonic errors using

1090-7807/99 $30.00

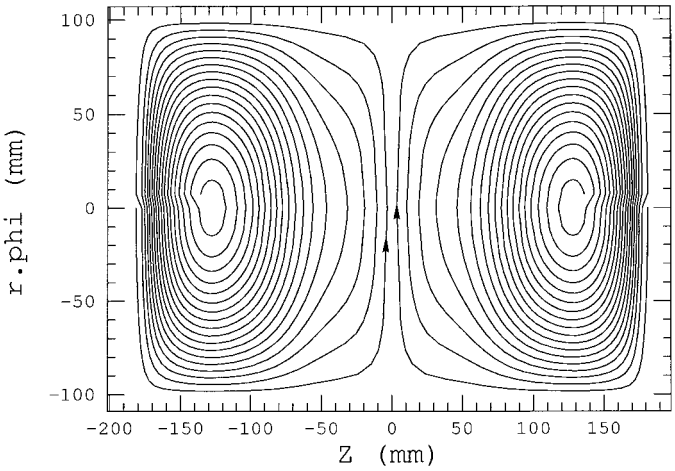

FIG. 1. One half of a transverse wire pattern. Y grad pattern knee coil.

simulated annealing (SA), which we, and others, have shown to be an effective design methodology for gradient coils (*12–14*). For SA optimization to be effective, a large number of iterations is required to locate the global minimum of the error space and descend to the lowest topology in the minimum. So that this process is not too time consuming, we have developed a computationally efficient algorithm for directly calculating the spherical harmonics generated by a thick arc of current carrying wires. This enabled the thousands of iterations necessary to design the gradient set to be completed in less than 2 h. In the Z-gradient design, the SA optimization proceeded by randomly adjusting the positions of the coil bundles, the number of turns in each bundle, the width of each bundle, and their radial extent. The error function for minimization was simply a weighted sum-of-squares of the magnitude of zonal and tesseral harmonics up to sixth order. Energy and/or power dissipation terms could also be included in the error function, as we have previously demonstrated (*9, 12*).

OUTLINE OF THE SPHERICAL HARMONIC CALCULATION METHOD

Consider then the multiturn arc of Fig. 3. The object is to directly and rapidly compute the spherical harmonics generated

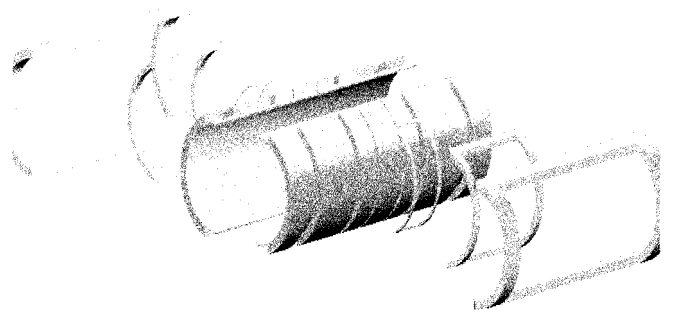

FIG. 2. The openable Z-gradient concept.

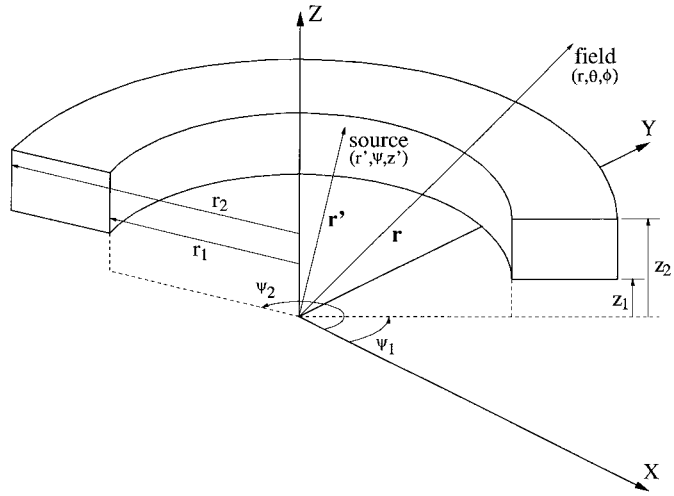

FIG. 3. Circular arc with rectangular cross-section. Indicated are a typical source point (within the coil) measured in cylindrical polar coordinates and a typical field point measured in spherical polar coordinates.

by the structure. We now present the main steps involved in the new calculation method. In a volume through which no current passes, the field at the point **r** is given by the expression

$$\mathbf{B}_z(\mathbf{r}) = \sum_n \sum_m r^n[a_{nm}\cos(m\phi) + b_{nm}\sin(m\phi)]P_{nm}(\cos\theta), \quad [1]$$

the spherical polar coordinate solution to Laplace's equation, where the polynomial $P_{nm}(\cos\theta)$, (order n, degree m) are solutions to the associated Legendre equation. The coefficients $r^n a_{nm}$ and $r^n b_{nm}$ are the magnitudes of the spherical harmonic

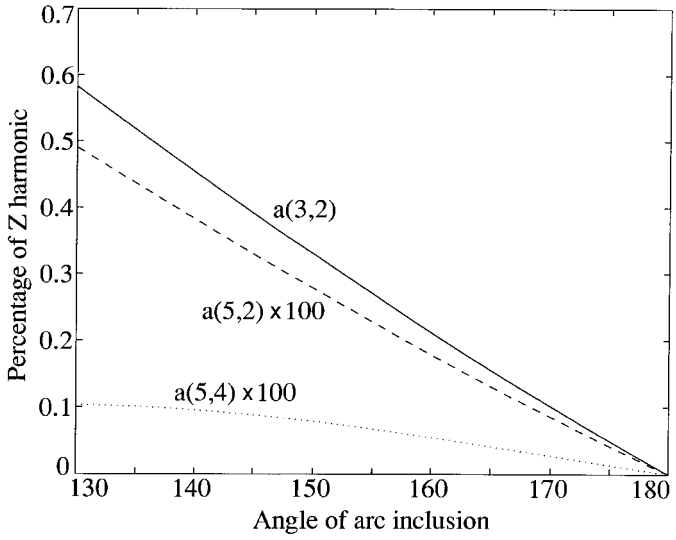

FIG. 4. The trend of significant tesseral harmonic impurities with inclusion angle.

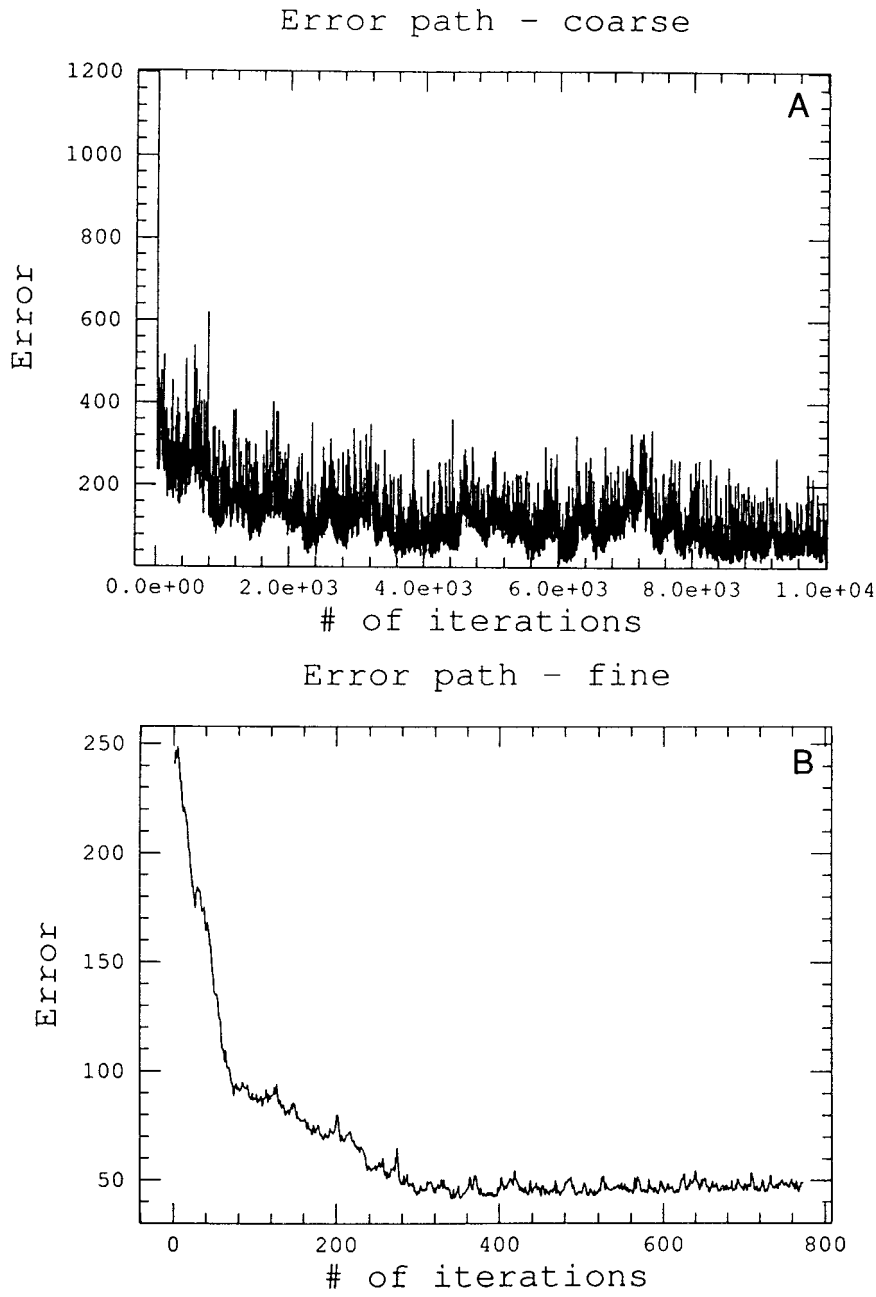

FIG. 5. The error paths of a typical optimization run in two parts: (A) coarse first run with limited iterations and (B) final run after overlapping coil coalescence.

terms. This equation is orthogonal for varying n and m values, a property which allows the expressions for the coefficients a_{nm} and b_{nm} to be obtained, for degree $m = 0$,

$$a_{n0} = r^{-n}\frac{2n+1}{4\pi}\int_{\phi=0}^{2\pi}\int_{\theta=0}^{\pi}\mathbf{B}_z(\mathbf{r})\,P_n(\cos\theta)\sin\theta\,d\theta d\phi,$$

$$b_{n0} = 0, \qquad [2]$$

for degree $m = 1, 2, 3, \ldots,$

$$a_{nm} = r^{-n}\frac{(2n+1)(n-m)!}{2\pi(n+m)!}\int_{\phi=0}^{2\pi}\int_{\theta=0}^{\pi}\mathbf{B}_z(\mathbf{r}) \times P_{nm}(\cos\theta)\sin\theta\,\cos(m\phi)\,d\theta d\phi,$$

$$b_{nm} = r^{-n}\frac{(2n+1)(n-m)!}{2\pi(n+m)!}\int_{\phi=0}^{2\pi}\int_{\theta=0}^{\pi}\mathbf{B}_z(\mathbf{r}) \times P_{nm}(\cos\theta)\sin\theta\,\sin(m\phi)\,d\theta d\phi. \qquad [3]$$

TABLE 1
Gz Coil Positions (One-Half Pattern)

Coil No.	Axial midpoint (mm)	Width of coil (mm)	Number of turns
1	7.6	1.8	1
2	63.2	3.6	2
3	159.6	30.6	17

Thus the spherical harmonics may be calculated when the field $\mathbf{B}_z$ is known.

The gradient coil is assumed to be composed of thick current carrying circular arc segments, producing a field of interest in the **z** direction. From Maxwell's equations, the magnetic induction **B** is given by

$$\mathbf{B}(\mathbf{r}) = \text{curl}\mathbf{A}(\mathbf{r}), \qquad [4]$$

where the vector potential **A**, in a medium with permeability μ, is given by the generalized Biot–Savart law

$$\mathbf{A}(\mathbf{r}) = \frac{\mu}{4\pi}\int\int\int_V \frac{\mathbf{J}(\mathbf{r}')}{|\mathbf{r}-\mathbf{r}'|}\,dV'. \qquad [5]$$

In this expression, the unprimed variables denote field points and primed variables source points (i.e., within the current-carrying arcs). Field points **r** are measured in spherical polar coordinates (r, θ, ϕ), corresponding to those in Eq. [1]. Source points $\mathbf{r}'$ are measured in cylindrical polar coordinates (r', ψ, z'), allowing a circular arc to be easily described. The constant current density J_0 directed around the arc gives

$$\mathbf{J}(\mathbf{r}') = \mathrm{J}_0\mathbf{e}_\psi, \qquad [6]$$

where $\mathbf{e}_\psi$ is the unit vector in the ψ direction. Relating both the spherical and the cylindrical coordinate system to the same Cartesian coordinate system, we may establish

$$\mathbf{e}_\psi = \sin\theta\,\sin(\phi-\psi)\mathbf{e}_r + \cos\theta\,\sin(\phi-\psi)\mathbf{e}_\theta + \cos(\phi-\psi)\mathbf{e}_\phi. \qquad [7]$$

Combining Eqs. [5]–[7], with the dimensions of the arc under consideration, gives an expression for the magnetic potential

$$\mathbf{A}(\mathbf{r}) = A_r\mathbf{e}_r + A_\theta\mathbf{e}_\theta + A_\phi\mathbf{e}_\phi, \qquad [8]$$

where the components in the r, θ, ϕ directions are given by

$$A_r = \frac{\mu J_o}{4\pi}\int_{\psi=\psi_1}^{\psi_2}\int_{r'=r_1}^{r_2}\int_{z'=z_1}^{z_2}\frac{\sin\theta\sin(\phi-\psi)}{|r-r'|}r'dz'dr'd\psi,$$

$$A_\theta = \frac{\mu J_o}{4\pi}\int_{\psi=\psi_1}^{\psi_2}\int_{r'=r_1}^{r_2}\int_{z'=z_1}^{z_2}\frac{\cos\theta\sin(\phi-\psi)}{|r-r'|}r'dz'dr'd\psi,$$

$$A_\phi = \frac{\mu J_o}{4\pi}\int_{\psi=\psi_1}^{\psi_2}\int_{r'=r_1}^{r_2}\int_{z'=z_1}^{z_2}\frac{\cos(\phi-\psi)}{|r-r'|}r'dz'dr'd\psi, \qquad [9]$$

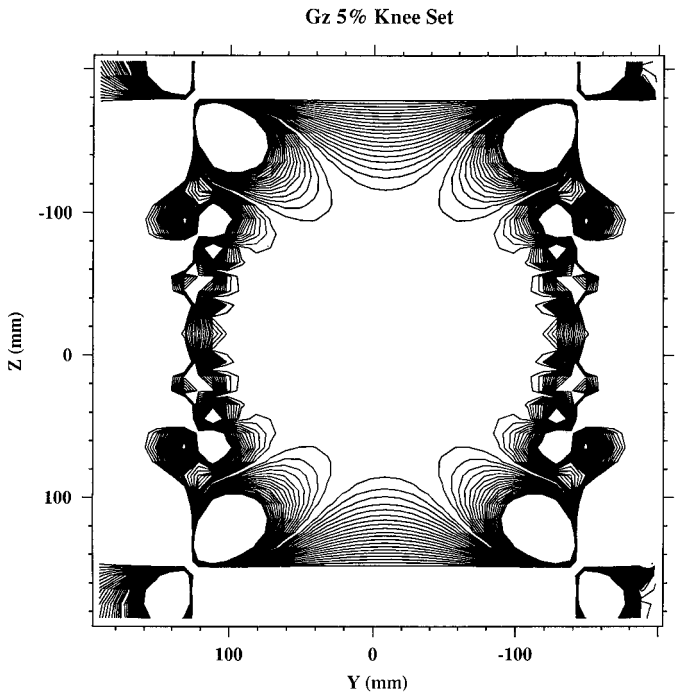

FIG. 6. The contour plot of the expected Z-gradient linearity in 5% contours, that is, the first contour is 5% from the central value, the second 10%, etc.

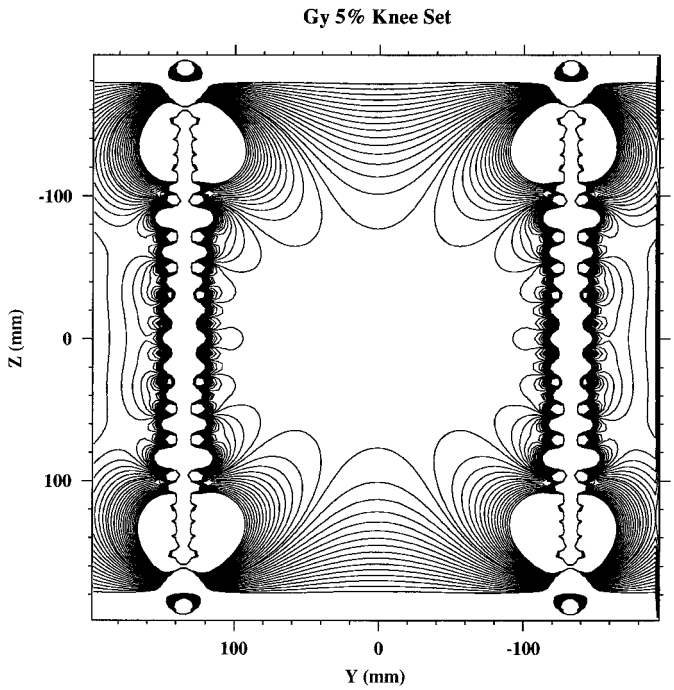

FIG. 7. The contour plot of the expected X-gradient linearity in 5% contours, that is, the first contour is 5% from the central value, the second 10%, etc.

FIG. 8. The prototype four-arc gradient set shown with the RF resonator closed (it is fully openable).

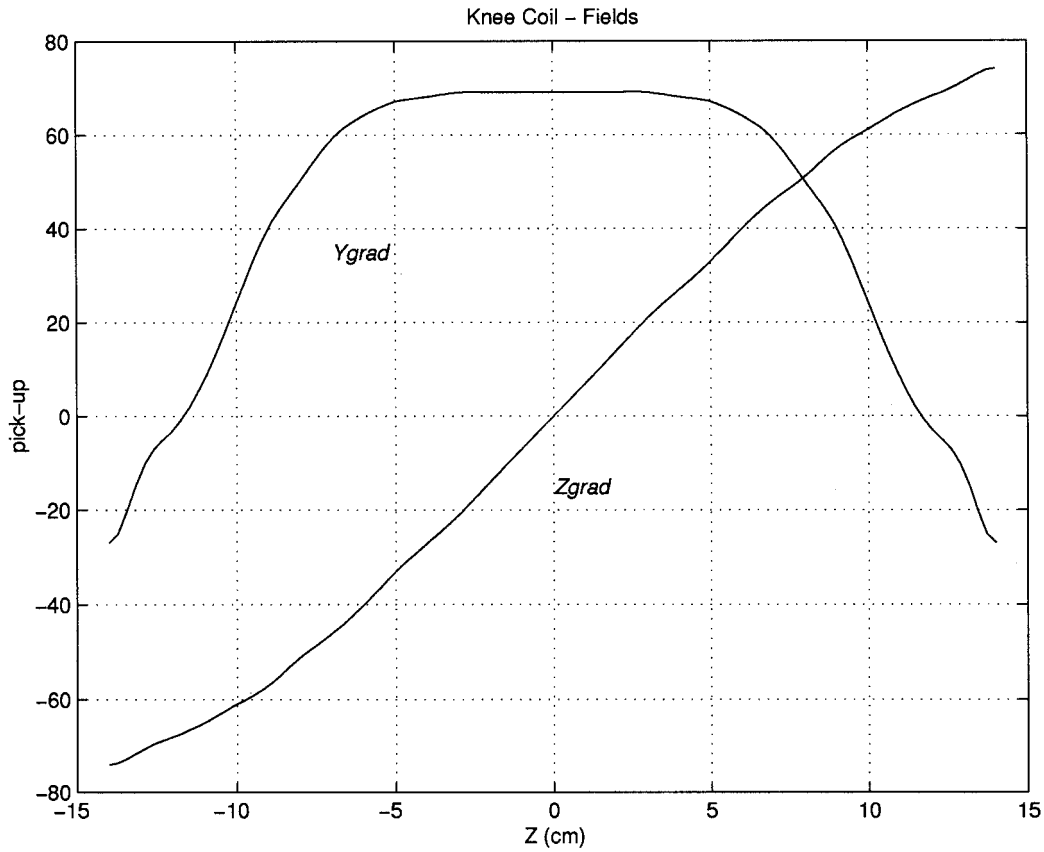

FIG. 9. The measured field generated by the Z and Y gradients along the Z axis. The 5% linear regions correspond to a dsv of 12 cm.

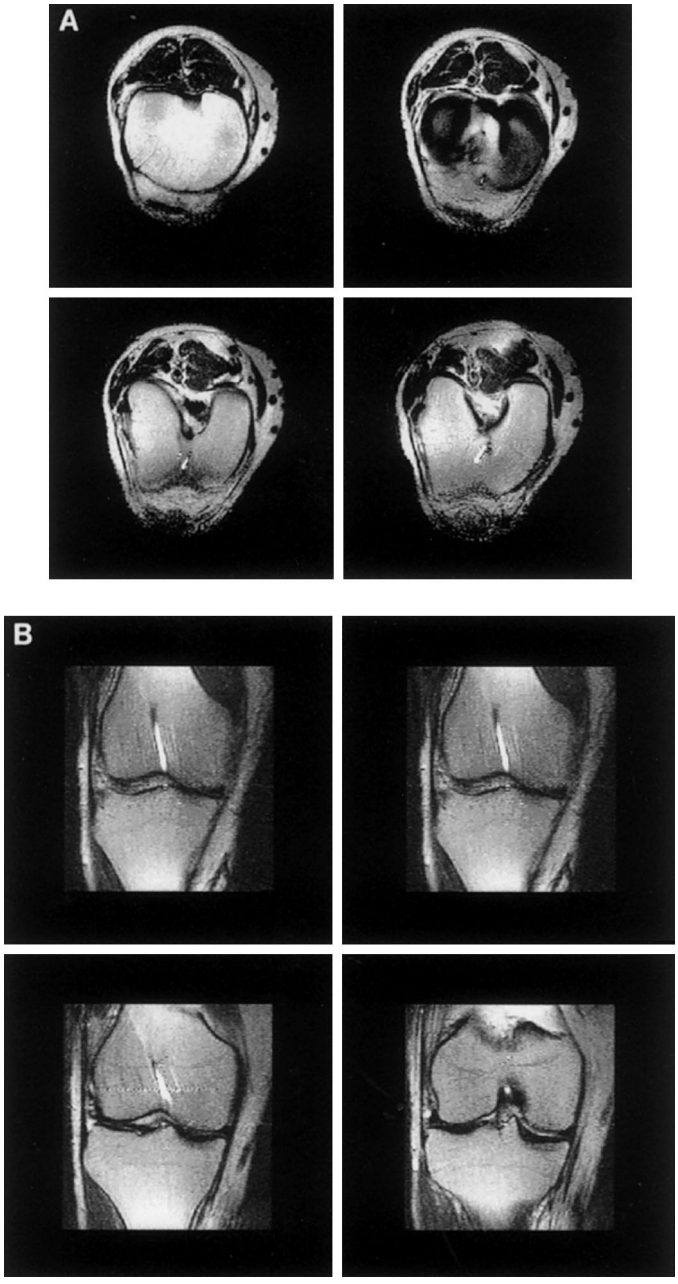

FIG. 10. (A) Transverse RARE images of the knee of a patient. The slice thickness was 4 mm, the FOV 150 mm, the acquisition matrix 256 × 256, the RARE factor 8, TR/TE = 3000/20 ms, and image acquisition required 4 min of signal averaging. Note the "cyst-like" appearance of an interosseus ganglion in the images due to an acute injury to the anterior cruciate ligament of the patient, generating the ganglion at the femoral insertion point of the ligament. This is more apparent in the coronal images of (B).

with the distances between the field and source points

$$|\mathbf{r} - \mathbf{r}'| = (r^2 + (r')^2 + (z')^2 - 2rz'\cos\theta - 2rr'\sin\theta\cos(\phi - \psi))^{1/2} = \sqrt{\alpha^2 + \beta^2 + \gamma^2},$$

where we define

$$\alpha = z' - r\cos\theta,$$

$$\beta = r\sin\theta\sin(\phi - \psi),$$

$$\gamma = r' - r\sin\theta\cos(\phi - \psi) = r' - \eta,$$

$$\eta = r\sin\theta\cos(\phi - \psi). \qquad [10]$$

Applying Eq. [4] and considering the unit direction vectors for the spherical polar coordinate system used allows an expression for the field in the z direction to be written

$$\mathbf{B}_z(\mathbf{r}) = \frac{\cos\theta}{r\sin\theta}\left(\frac{\partial}{\partial\theta}(\sin\theta A_\phi) - \frac{\partial A_\theta}{\partial\phi}\right) - \frac{1}{r}\left(\frac{\partial A_r}{\partial\phi} - \sin\theta\frac{\partial}{\partial r}(rA_\phi)\right). \qquad [11]$$

Thus we may calculate the coefficients a_{nm} and b_{nm} by substituting Eqs. [9]–[11] into Eqs. [2] and [3]. On substitution it becomes possible to complete three of the resulting five integrals in closed form, specifically those in ψ, r', z'. With only two integrals remaining, and the dimensions of the current carrying arcs merely variables in the method, the spherical harmonics may be evaluated quickly and accurately by numerical techniques. The details of completing the integrals are extensive and the final results complicated (although they only involve simple functions). Some of the resultant expressions are derived in the Appendix and complete details may be found in (*15*). This algorithm is useful in areas of NMR magnetostatic analysis and design other than gradient coils, such as magnet and shim coils, and in unrelated areas such as magnetohydrodynamics and magnetic "bottles."

We have compared our method with test cases where each wire in the coil-arc is discretized, the field is calculated explicitly using Biot–Savart summations, and the spherical harmonics are deconvolved from the field. Depending on the number of wires in the gradient coil, our method is between one and two orders of magnitude faster than the traditional alternative (*15*). These computational speed improvements are very important for stochastic optimization methods.

The effect of the axial return paths in the Z gradient is, in effect, to restrict the azimuthal inclusion angle of the "B_z-active" arcs. So that we can choose a suitable maximum return path width, we need to quantify the effect of varying the inclusion angle with resultant homogeneity. We might reasonably expect that the terms generated by increasing the thickness of the return paths would be tesseral and should be zero with a complete azimuthal coverage, increasing as the inclusion angle decreases. This is exactly what is observed in Fig. 4, where we note that the major contaminant is

$a_{3,2}$, with $a_{5,2}$ and $a_{5,4}$ also increasing but smaller than $a_{3,2}$.

The optimization process proceeded by minimizing an error function including all odd order zonal terms as well as $a_{3,2}$, $a_{5.2}$, and $a_{5,4}$ using a standard SA algorithm with adaptive step sizing (*11–13*). Each SA run took about 2 h to complete and consisted of a coarse run with relatively large step sizes for each of the parameters, followed by a fine run with considerably smaller step sizes. The algorithm coalesced the 10-coil starting point to a 6-coil result. The error paths to a "frozen" state are shown in Fig. 5. Details of one-half of the final coil configuration are given in Table 1; 1.8-mm annealed copper wire was laid into a fiberglass substrate with 18-mm-wide return paths running axially. The resultant significant contaminants for the final design, relative to the desired harmonic, over a 12-cm dsv were Z3 (3e–3%), Z5(−9e–2%), Z7(−5.5e–2%), Z(x^2–y^2) (0.2%).

Similarly for the Y-gradient coil, shown in part in Fig. 1, over a 12-cm dsv, the only significant impurity harmonic was approximately 0.9% of Z^2X. Figures 6 and 7 show the predicted 5% contour lines of the longitudinal and transverse gradients, respectively, indicating that all should be linear to at least 5% over the desired 12-cm central region.

RESULTS AND DISCUSSION

A three-axis gradient set was constructed and interfaced to a 2-T OMT magnet system. The driving console was a Bruker Avance. The "4-arc" construction of the set shown in Fig. 8 consisted of an inner pair containing the Y gradient and an outer pair containing the X and Z gradients. The transverse gradients were constructed by laser cutting copper sheets in a streamline pattern and the longitudinal coil by laying wires in predetermined tracks. A small pick-up coil was used to assess the linearity of the gradients—Fig. 9 shows typical plots and indicates the useful linear region to be 12–14 cm. This was confirmed by phantom images.

The complete electrical characteristics of the constructed gradient set were

	R(Ω)/L(μH)	Sensitivity (mT/m/A)	5% Linear region (cm)
X	0.48/120.0	1.05	12
Y	0.46/110.0	1.2	12
Z	0.5/280.0	0.96	12

The set was mounted 3 cm off-center in the x direction in a 2-T (OMT) MRI system (Bruker). A 300-V 50-amp Copley amplifier was used to drive the set up to 6 G/cm (60 mT/m); all preemphasis and $\mathbf{B}_0$ compensations were small (<5%). Switching times for all gradients were less than 110 μs. The gradient set is torque-balanced, due to its symmetry of construction, and did not demonstrate any appreciate motion when it was pulsed after the removal of mounting fixtures. Splitting the set to make it openable clearly reduces the strength of the structure, but providing the hinges and lock-down structures are durable, and the symmetry of the structure is retained, the openable set handles the forces of gradient pulsing without problems.

The RF resonator used in the experiments was a linearly polarized split high-pass design, fed so that the splitting did not interfere with the rungs (*16, 17*). A double-sided, slotted shield is used on the RF resonator which is used both as a transmitter and as a receiver coil.

Figures 10a and 10b show transverse and coronal RARE images of a knee joint acquired using the system. In each case the slice thickness was 4 mm, the FOV 150 mm, the acquisition matrix 256 × 256, the RARE factor 8, TR/TE = 3000/20 ms, and image acquisition required 4 min of signal averaging. Note the "cyst-like" appearance of an interosseus ganglion in the images due to an acute injury to the anterior cruciate ligament of the patient, generating the ganglion at the femoral insertion point of the ligament.

CONCLUSION

A high-strength local gradient set has been designed and constructed for orthopedic MRI that allows unprecedented access for patients with restricted joint mobility. The design of the longitudinal set is presented in detail and contains a new algorithm for directly calculating the spherical harmonics of a thick arc of current-carrying wire. The new calculation method has a number of applications in electromagnetics. The complete gradient set performed as predicted by theory.

APPENDIX

After substituting Eqs. [9]–[11] into Eqs. [2] and [3], the expression for the harmonic coefficients may be expressed as, for degree $m = 0$,

$$a_{n0} = r^{-(n+1)} \frac{(2n+1)}{4\pi} \frac{\mu J_0}{4\pi} (E_{n0}^{(1)} - E_{n0}^{(2)} - E_{n0}^{(3)} + E_{n0}^{(4)})$$

$$b_{n0} = 0, \qquad \text{[A1]}$$

similarly for degree $m = 1, 2, 3, \ldots,$

$$a_{nm} = r^{-(n+1)} \frac{(2n+1)(n-m)!}{2\pi(n+m)!} \frac{\mu J_0}{4\pi} \times (E_{nm}^{(1)} - E_{nm}^{(2)} - E_{nm}^{(3)} + E_{nm}^{(4)})$$

$$b_{nm} = r^{-(n+1)} \frac{(2n+1)(n-m)!}{2\pi(n+m)!} \frac{\mu J_0}{4\pi} \times (F^{(1)}_{nm} - F^{(2)}_{nm} - F^{(3)}_{nm} + F^{(4)}_{nm}), \quad [A2]$$

where

$$E^{(1)}_{nm} = \int_{\phi=0}^{2\pi} \int_{\theta=0}^{\pi} \frac{\partial}{\partial\theta} [\sin\theta \int_{\psi=\psi_1}^{\psi_2} \cos(\phi - \psi) \mathbb{N}(r, \theta, \phi; \psi) d\psi] \times \cos\theta P_{nm}(\cos\theta)\cos(m\phi) d\theta d\phi,$$

$$E^{(2)}_{nm} = \int_{\phi=0}^{2\pi} \int_{\theta=0}^{\pi} \frac{\partial}{\partial\phi} [\int_{\psi=\psi_1}^{\psi_2} \sin(\phi - \psi) \mathbb{N}(r, \theta, \phi; \psi) d\psi] \times \cos^2\theta P_{nm}(\cos\theta)\cos(m\phi) d\theta d\phi,$$

$$E^{(3)}_{nm} = \int_{\phi=0}^{2\pi} \int_{\theta=0}^{\pi} \frac{\partial}{\partial\phi} [\int_{\psi=\psi_1}^{\psi_2} \sin(\phi - \psi) \mathbb{N}(r, \theta, \phi; \psi) d\psi] \times \sin^2\theta P_{nm}(\cos\theta)\cos(m\phi) d\theta d\phi,$$

$$E^{(4)}_{nm} = \int_{\phi=0}^{2\pi} \int_{\theta=0}^{\pi} \frac{\partial}{\partial r} [r \int_{\psi=\psi_1}^{\psi_2} \cos(\phi - \psi) \mathbb{N}(r, \theta, \phi; \psi) d\psi] \times \sin^2\theta P_{nm}(\cos\theta)\cos(m\phi) d\theta d\phi. \quad [A3]$$

The constants F_{nm} appearing in Eq. [A2] have the same form as [A3], with $\cos(m\phi)$ replaced by $\sin(m\phi)$. Also we define for convenience

$$\mathbb{N}(r, \theta, \phi; \psi) = \int_{r'=r_1}^{r_2} \int_{z'=z_1}^{z_2} \frac{r' dz' dr'}{\sqrt{\alpha^2 + \beta^2 + \gamma^2}}. \quad [A4]$$

Combining Eqs. [A3] and [A4], we have five integrals to solve. After a considerable amount of algebra (*15*), we may solve three of the five integrals in closed form. The solutions for E_{nm} (and therefore a_{nm}) are

$$E^{(1)}_{nm} = \frac{1}{2m} \int_{\phi=0}^{2\pi} \int_{\theta=0}^{\pi} \cos\phi[\sin(m(\phi + \psi_2)) - \sin(m(\phi + \psi_1))] \times [\mathbb{C}(r, \theta, \phi; r_2, 0, z_2) - \mathbb{C}(r, \theta, \phi; r_1, 0, z_2) - \mathbb{C}(r, \theta, \phi; r_2, 0, z_1) + \mathbb{C}(r, \theta, \phi; r_1, 0, z_1)] \times [\cos\theta \sin\theta P_{n,m+1}(\cos\theta) + (\sin^2\theta - m\cos^2\theta) P_{nm}(\cos\theta)] d\theta d\phi,$$

$$E^{(2)}_{nm} = \frac{1}{2} \int_{\phi=0}^{2\pi} \int_{\theta=0}^{\pi} [\sin(\phi - \psi_1) \times [\mathbb{C}(r, \theta, \phi; r_2, \psi_1, z_2) - \mathbb{C}(r, \theta, \phi; r_1, \psi_1, z_2) - \mathbb{C}(r, \theta, \phi; r_2, \psi_1, z_1) + \mathbb{C}(r, \theta, \phi; r_1, \psi_1, z_1)] - \sin(\phi - \psi_2) \times [\mathbb{C}(r, \theta, \phi; r_2, \psi_2, z_2) - \mathbb{C}(r, \theta, \phi; r_1, \psi_2, z_2) - \mathbb{C}(r, \theta, \phi; r_2, \psi_2, z_1) + \mathbb{C}(r, \theta, \phi; r_1, \psi_2, z_1)]] \times [\cos^2\theta P_{nm}(\cos\theta)\cos(m\phi)] d\theta d\phi,$$

$$E^{(3)}_{nm} = \frac{1}{2} \int_{\phi=0}^{2\pi} \int_{\theta=0}^{\pi} [\sin(\phi - \psi_1) \times [\mathbb{C}(r, \theta, \phi; r_2, \psi_1, z_2) - \mathbb{C}(r, \theta, \phi; r_1, \psi_1, z_2) - \mathbb{C}(r, \theta, \phi; r_2, \psi_1, z_1) + \mathbb{C}(r, \theta, \phi; r_1, \psi_1, z_1)] - \sin(\phi - \psi_2) \times [\mathbb{C}(r, \theta, \phi; r_2, \psi_2, z_2) - \mathbb{C}(r, \theta, \phi; r_1, \psi_2, z_2) - \mathbb{C}(r, \theta, \phi; r_2, \psi_2, z_1) + \mathbb{C}(r, \theta, \phi; r_1, \psi_2, z_1)]] \times [\sin^2\theta P_{nm}(\cos\theta)\cos(m\phi)] d\theta d\phi,$$

$$E^{(4)}_{nm} = \frac{1}{2m} \int_{\phi=0}^{2\pi} \int_{\theta=0}^{\pi} \cos\phi[\sin(m(\phi + \psi_2)) - \sin(m(\phi + \psi_1))] \times [\mathbb{I}(r, \theta, \phi; r_2, 0, z_2) - \mathbb{I}(r, \theta, \phi; r_1, 0, z_2) - \mathbb{I}(r, \theta, \phi; r_2, 0, z_1) + \mathbb{I}(r, \theta, \phi; r_1, 0, z_1)] \times [\sin^2\theta P_{nm}(\cos\theta)] d\theta d\phi. \quad [A5]$$

Likewise, the components F_{nm}, of the coefficients b_{nm}, may be expressed by formulae involving integrals in only two variables, which may be rapidly and accurately evaluated using Gauss–Legendre quadrature.

In Eqs. [A5] above it has been convenient to define the expressions

$$\mathbb{C}(r, \theta, \phi; r', \psi, z') = \alpha\sqrt{\alpha^2 + \beta^2 + \gamma^2} + (\beta^2 + (r')^2 - \eta^2)\ln|\alpha + \sqrt{\alpha^2 + \beta^2 + \gamma^2}| + 2\eta\alpha \ln|\gamma + \sqrt{\alpha^2 + \beta^2 + \gamma^2}| + 4\eta\beta \arctan\left(\frac{\alpha + \gamma + \sqrt{\alpha^2 + \beta^2 + \gamma^2}}{\beta}\right) \quad [A6]$$

$$\mathbb{I}(r,\theta,\phi;r'\psi,z') = \mathbb{C}(r,\theta,\phi;r',\psi,z') - r\cos\theta\sqrt{\alpha^2+\beta^2+\gamma^2} + 2(\beta^2-\eta^2)\ln|\alpha+\sqrt{\alpha^2+\beta^2+\gamma^2}|$$
$$+ 2\eta(\alpha - r\cos\theta)\ln|\gamma+\sqrt{\alpha^2+\beta^2+\gamma^2}| + 8\eta\beta\arctan\left(\frac{\alpha+\gamma+\sqrt{\alpha^2+\beta^2+\gamma^2}}{\beta}\right)$$
$$+ \frac{(\beta^2-\eta^2)(\alpha-r\cos\theta) - \alpha\eta r' - r\cos\theta(\alpha^2+(r')^2)}{\sqrt{\alpha^2+\beta^2+\gamma^2}}$$
$$+ \frac{(\beta^2+(r')^2-\eta^2)(\beta^2-\eta\gamma)}{\sqrt{\alpha^2+\beta^2+\gamma^2}(\alpha+\sqrt{\alpha^2+\beta^2+\gamma^2})} + \frac{2\eta\alpha(\beta^2-r\cos\theta\alpha)}{\sqrt{\alpha^2+\beta^2+\gamma^2}(\gamma+\sqrt{\alpha^2+\beta^2+\gamma^2})}$$
$$+ \frac{2\eta\beta^2(\alpha z' + \gamma r' + (z'+r')\sqrt{\alpha^2+\beta^2+\gamma^2})}{\sqrt{\alpha^2+\beta^2+\gamma^2}(\gamma+\sqrt{\alpha^2+\beta^2+\gamma^2})(\alpha+\sqrt{\alpha^2+\beta^2+\gamma^2})}. \qquad [A7]$$

ACKNOWLEDGMENTS

We thank Drs. Graham Galloway and Stephen Rose for assistance with the imaging experiments, Gavin Hinds, Nick Mills, Paul McCarragher, and Simon Teed for their involvement in constructing the gradient set, and The Australian Research Council for financial support.

REFERENCES

1. R. Turner, D. Le Bihan, J. Maier, R. Vavrek, L. K. Hedges, and J. Pekar, *Radiology* **177,** 407 (1990).
2. E. Wong, *in* "Encyclopaedia of Nuclear Magnetic Resonance" (D. M. Grant and R. K. Harris, Eds.), pp. 5015–5020, Wiley, London (1996).
3. P. J. Basser, J. Mattiello, and D. Le Bihan, *Biophys. J.* **66,** 259 (1994).
4. J. Hennig, A. Nauerth, and H. Friedburg, *Magn. Reson. Med.* **3,** 823 (1986).
5. P. Mansfield, *J. Phys. C.* **10,** L55 (1977).
6. S. Crozier, W. U. Roffmann, K. Luscher, G. Hinds, N. Mills, P. McCarragher, S. Teed, and D. M. Doddrell, Proceedings of the International Society for Magnetic Resonance in Medicine, Sixth Scientific Meeting, Sydney, p. 52 (1998).
7. R. Turner, *Magn. Reson. Imag.* **11,** 903 (1993).
8. C. D. Eccles, S. Crozier, M. Westphal, and D. M. Doddrell, *J. Magn. Reson.* **103,** 135 (1993).
9. S. Crozier, S. Dodd, and D. M. Doddrell, *Meas. Sci. Technol.* **36** (1996).
10. M. W. Garrett, *J. Appl. Phys.* **22,** 1091 (1951).
11. M. W. Garrett, *J. Appl. Phys.* **38,** 2563 (1967).
12. S. Crozier, and D. M. Doddrell, *J. Magn. Reson.* **103,** 354 (1993).
13. S. Crozier, L. K. Forbes, and D. M. Doddrell, *J. Magn. Reson.* **107,** 126 (1994).
14. M. L. Buszko, M. F. Kempka, E. Szezesniak, D. C. Wang, and E. R. Andrews, *J. Magn. Reson.* **112,** 207 (1996).
15. C. J. Snape-Jenkinson, L. K. Forbes, and S. Crozier, *IEEE. Trans. Magn.* in press (1999).
16. S. Crozier, K. Luescher, L. K. Forbes, and D. M. Doddrell, *J. Magn. Reson. B* **109,** 1 (1995).
17. C. E. Hayes, W. A. Edelstein, J. F. Schenck, O. M. Muller and M. Eash, *J. Magn. Reson.* **63,** 622 (1985).